INORGANIC CHEMISTRY FRONTIERS

RESEARCH ARTICLE

View Article Online
View Journal | View Issue



Cite this: *Inorg. Chem. Front.*, 2025, **12**, 8315

# Beyond monofunctionality: a pyridinium-derived photochromic Zn-MOF with tetracycline detection/degradation and its Eu/Tb hybrids for visual monitoring and multi-level security

Jian-Hua Xue,†[a] Dong-Dong Yang, *†[a] Yong-Sheng Shi,[b] Yuan-Yu Yang,[a] Yu-Jia Bai,[a] Qi Ma *[a,c] and Xiang-Jun Zheng *[d]

Although progress has been made in recognizing and degrading tetracyclines (TC), integrating multiple functions—including specificity, intrinsic photoresponsive behavior, targeted pollutant recognition/degradation, and designable luminescence—within a single MOF platform remains a significant challenge. Most reported systems excel in specific functions but lack synergistic integration. To address this gap, the rational synthesis and multifunctional exploration of a novel zinc-based MOF (complex **1**) was reported. Complex **1** successfully integrates photochromism with TC management functions, enabling fluorescence sensing (LOD = 0.72 μM) while achieving efficient degradation and adsorption (88.08%) driven by π–π stacking interactions, pore confinement and photoelectron transfer. To enhance functionality, post-synthetic modification (PSM) was employed to incorporate $Eu^{3+}$/$Tb^{3+}$ ions into complex **1**, yielding **Eu/Tb@Zn-MOFs** hybrids. Strikingly, the $Eu^{3+}$/$Tb^{3+}$ doping preserved the parent complex's photochromic properties while introducing characteristic f–f luminescence, enabling dual photochromic-fluorescent responses. By bridging pyridinium-ligand chemistry with MOF-based rare-earth functionalization, this study advances the design of multi-responsive coordination materials. The synergistic integration of photochromism, luminescence and structural durability provides a versatile platform for next-generation anti-counterfeit technologies, fluorescence detection, dynamic optics and stimuli-responsive smart materials. This work provides a metal-specific design strategy for multi-stimuli-responsive materials and pioneers a modular approach to advanced anti-counterfeiting and environmental remediation technologies.

Received 4th August 2025,
Accepted 6th September 2025

DOI: 10.1039/d5qi01641j

rsc.li/frontiers-inorganic



## 1. Introduction

Tetracycline (TC), a widely used broad-spectrum antibiotic, poses significant environmental risks. Over 70% of administered TC is excreted unmetabolized into aquatic systems *via* urine and feces.[1–4] Consequently, TC residues are routinely detected in surface water, groundwater, and even drinking water, threatening ecosystems and human health at trace levels.[5] This necessitates materials capable of both sensitive detection and effective degradation of TC. Fluorescence detection offers advantages (portability, low cost, speed) over conventional methods (*e.g.*, HPLC, ELISA),[6–8] yet achieving simple visual readout remains challenging.[9] For degradation, photocatalysis surpasses traditional approaches (adsorption, AOPs) in efficiency and eco-friendliness.[10–12] In the search for efficient photocatalytic TC degradation, various materials such as MOFs, COFs, LDHs, and CDs have been studied. Each material family exhibits distinct characteristics: COFs are known for their high stability and designable porous structures,[13] LDHs for their tunable layered architectures and rich redox chemistry,[14] and CDs for their strong light absorption and electron transfer capabilities.[15,16] However, these materials often face limitations such as insufficient active sites, limited light absorption, or rapid charge recombination. In contrast, MOFs offer exceptional structural versatility, ultra-high surface areas, and finely tunable chemical environments, making them highly promising as photocatalysts.[17] Specifically, for a Zn-based MOF to achieve high-performance

[a]*School of Chemistry and Chemical Engineering, Shanxi Datong University, Datong 037009, China. E-mail: ddyang@sxdtdx.edu.cn*
[b]*College of Chemistry and Chemical Engineering, Jiangxi Science and Technology Normal University, Nanchang 330013, China*
[c]*Department of Chemistry, Xinzhou Teachers University, Xinzhou, Shanxi, 034000, China. E-mail: maqihx@163.com*
[d]*Beijing Key Laboratory of Energy Conversion and Storage Materials, College of Chemistry, Beijing Normal University, Beijing 100875, China. E-mail: xjzheng@bnu.edu.cn*
†These authors contributed equally to this work.

photocatalytic degradation of TC, it should ideally possess the following attributes: strong visible-light absorption through ligand design or metal-node coordination, efficient photo-induced charge separation and migration to minimize recombination, abundant exposed active sites for reactant adsorption and activation, and excellent chemical stability in the aqueous reaction environment.[18]

Stimuli-responsive smart materials capable of reversibly modulating optical properties under external triggers (*e.g.*, light, heat, mechanical force) have attracted significant interest in recent decades, particularly for applications in information encryption, sensors, and optoelectronics.[19,20] Among these, photochromic materials hold substantial promise.[21–24] However, achieving robust multi-level anti-counterfeiting within a single system remains challenging, as it necessitates specific, sequential decryption stimuli (*e.g.*, time and light) to prevent unauthorized interpretation and replication.[25,26] Pyridinium-based ligands, featuring conjugated π-systems and proton-transfer capabilities electron-deficient capabilities are prominent building blocks for optically and thermally active materials. Their ability to mediate intramolecular charge transfer (ICT) and photogenerated radical dynamics underpins their utility.[27–29] Concurrently, lanthanide-functionalized metal–organic frameworks (Ln@MOFs) represent a paradigm for luminescent smart materials. Ions like $Eu^{3+}$ and $Tb^{3+}$ offer unique advantages—sharp emission lines, long lifetimes, and high color purity—making them ideal for optical encoding and anti-counterfeiting.[30–34] However, direct $Ln^{3+}$ incorporation during MOF synthesis is often hampered by coordination mismatches or inefficient energy transfer. Post-synthetic modification (PSM) offers a versatile solution, anchoring $Ln^{3+}$ ions into pre-formed MOF hosts while preserving intrinsic functionality.[35] Pyridinium-based zwitterionic MOFs have recently emerged as particularly promising hosts for PSM with $Ln^{3+}$ ions. Their charged frameworks facilitate $Ln^{3+}$ integration, and their photoactive ligands can act as antennas, harvesting light and transferring energy to $Ln^{3+}$ ions *via* LMCT or FRET mechanisms.[36,37] Despite these synergistic advantages, exploiting this strategy to create stimuli-responsive Ln@MOFs that dynamically modulate both color and emission intensity under external triggers—essential for advanced anti-counterfeiting and multi-level encryption—remains largely unexplored.

Herein, we report the rational design and synthesis of a novel coordination complex, $\{[Zn(cbby)]\cdot H_2O\}_n$ (**1**), assembled from $Zn^{2+}$ ions and the pyridinium-based ligand 5-(1-(3-carboxybenzyl)pyridin-4-yl)isophthalic acid ($H_3$cbby) (Scheme 1). Complex **1** exhibits intriguing photochromic behavior, attributed to electron transfer. Remarkably, complex **1** demonstrates unprecedented simultaneous sensing, adsorption and photodegradation of TC. The suspension of complex **1** maintained good stability and showed obvious luminescence quenching after gradual addition of TC, achieving a detection limit of 0.72 μM. This sensing capability, coupled with efficient adsorption and photocatalytic degradation (88.08% efficiency), arises synergistically from π–π stacking interactions between TC and the framework's benzene/pyridine rings, optimal pore size matching, and photogenerated electron transfer. In addition, leveraging the inherent porosity of this Zn-based framework, we performed post-synthetic modification (PSM) by anchoring $Eu^{3+}$/$Tb^{3+}$ ions, yielding lanthanide-incorporated materials denoted as **Eu/Tb@Zn-MOF**. Crucially, **Eu/Tb@Zn-MOF** retains the photochromic properties and high TC degradation efficiency of the parent framework. Building upon this multifunctionality, a detection platform for visual detection of TC is developed by using the color features of **Eu/Tb@Zn-MOF**. Moreover, a hierarchical anti-counterfeiting platform integrating **1** and **Eu/Tb@Zn-MOF** was developed. This platform enables multi-level authentication through orthogonal luminescent responses to specific stimuli (light irradiation, time evolution and UV observation).

## 2. Experimental section

### 2.1 Synthesis of $\{[Zn(cbby)]\cdot H_2O\}_n$ (1)

A mixture of $Zn(NO_3)_2\cdot 4H_2O$ (31 mg, 0.1 mmol), 5-(1-(3-carboxybenzyl)pyridin-4-yl)isophthalic acid ($H_3$cbby) (41 mg, 0.1 mmol), and DMF–$H_2O$ (5 : 1, v/v, 6 mL) was placed in a PTFE lined stainless steel vessel (25 mL) under self-pressurization and 100 °C for 3 days to obtain light yellow crystals. The reaction yield was about 60% with Zn as the raw material. Elemental analysis: calcd for $C_{21}H_{15}NO_7Zn$: C, 54.98; H, 3.30; N, 3.05%. Found: C, 54.81; H, 3.18; N, 3.16%. IR (KBr, $cm^{-1}$): 3423 s, 3124 w, 3066 w, 1631 s, 1562 m, 1392 s, 1290 w, 1216 w, 1151 w, 863 w, 750 w, 721 w.

### 2.2 Synthesis of Eu/Tb@Zn-MOF

Crystal **1** (30 mg) was dispersed in 10 mL of methanol solution containing $10^{-2}$ mol $L^{-1}$ $Eu(NO_3)_3\cdot 6H_2O$/$Tb(NO_3)_3\cdot 6H_2O$. After continuous stirring of the mixture at room temperature for 24 h, the resulting white powder was washed several times with methanol and centrifuged to produce **Eu/Tb@Zn-MOF**.

### 2.3 X-ray diffraction analysis

The single-crystal X-ray diffraction data of conformationally changed crystals of complex **1** was collected on an XtaLAB Synergy-DW diffractometer with Cu-Kα radiation ($\lambda$ = 0.71073 Å) at room temperature. The crystal structures were solved and refined using the Olex2 program and all hydrogen atoms were added automatically. Absorption corrections were applied by the program SADABS. All hydrogen atoms were added automatically and non-hydrogen atoms were refined anisotropically. Crystal data and structure refinement parameters are summarized in Table S1. Selected bond distances (Å) and angles (degree) are displayed in Table S2.

## 3. Results and discussion

### 3.1 The characterization of materials

The experimental powder X-ray diffraction (PXRD) pattern of complex **1** matches well with the simulatedone, confirming its

 

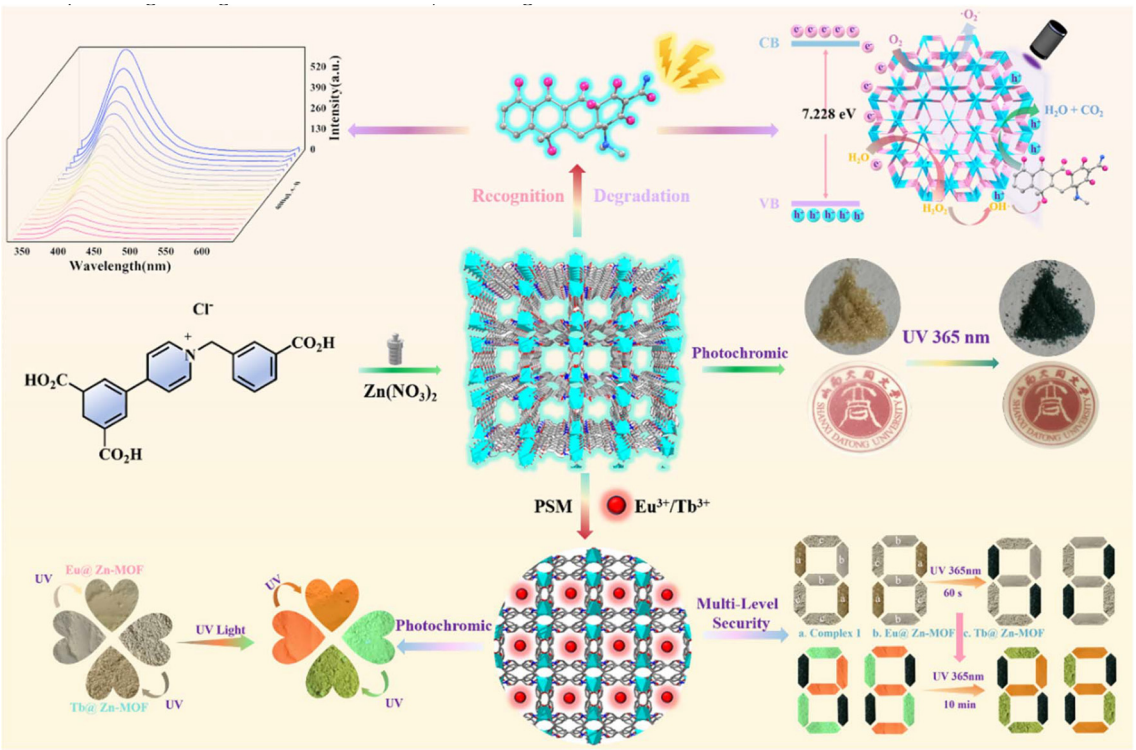


**Scheme 1** Schematic representation for constructing multifunctional stimuli-responsive **1** and **Eu/Tb@Zn-MOF**.

phase purity and structural integrity (Fig. S1). Post-synthetic modification of the complex **1** powder with $Eu^{3+}/Tb^{3+}$ ions was also characterized. As shown in Fig. S2, the modified material retains the framework's Bragg diffraction positions with only minor peak intensity variations, likely due to altered electron density, confirming successful encapsulation of the $Eu^{3+}/Tb^{3+}$ ions. TGA analysis (Fig. S3) reveals an 8.1% weight loss between 30–150 °C, corresponding to the release of one disordered $H_2O$ molecule (calcd: 7.84%). Framework decomposition occurs between 350–600 °C.

SEM analysis of complex **1** and its $Eu^{3+}/Tb^{3+}$-modified analogues reveals their morphology (Fig. S4). Both materials exhibit 1–50 μm block-like structures (Fig. S4a–4i), with the modified complexes retaining the original framework morphology, consistent with XRD data. However, their surfaces appear rougher, indicating successful $Eu^{3+}/Tb^{3+}$ incorporation. EDS mapping further confirms uniform elemental distribution (Fig. S4–S6). $N_2$ adsorption–desorption measurements show complex **1** has a BET surface area of 5.1320 $m^2\ g^{-1}$ and a maximum pore size of 150 nm (Fig. S7), classifying it as a macroporous solid.

### 3.2 Structural analysis and discussion

Single-crystal X-ray diffraction analysis reveals that the complex **1** crystallizes in the monoclinic system with space group *P*2/*c* (Table S1). The asymmetric unit consists of one $Zn^{2+}$ ion, one deprotonated $cbby^{2-}$ ligand and one lattice $H_2O$ molecule (Fig. 1a). The Zn1 atom is four-coordinated and forms a distorted tetrahedral [$ZnO_4$] geometry, which is completed by four oxygen atoms from four carboxylate groups from the four $cbby^{2-}$ ligands. The Zn1–O bond lengths range from 1.926(3) to 1.987(3) Å and the O–Zn1–O angles are within the range of 99.63(14)–122.99(15) (Table S2). Notably, every $cbby^{2-}$ ligand connects four Zn atoms with $\mu_4$-($k^1$–$k^1$)–($k^1$–$k^0$)–($k^1$–$k^0$)-coordination mode to form a 2D layered structure (Fig. 1b). The 2D network is further connected along the *c*-axis direction *via* $cbby^{2-}$ ligand to form a three-dimensional (3D) framework structure (Fig. 1c). Topological analysis using TOPOS software identifies the network as a 3,6-connected topology (Point Symbol: $\{4^2{\cdot}6\}^2\{4^4{\cdot}6^2{\cdot}8^8{\cdot}10\}$), where $Zn^{2+}$ acts as a 6-connected node and the $cbby^{2-}$ ligand serves as a 3-connected node (Fig. 1d). The framework exhibits a calculated solvent-accessible volume of 28% (PLATON),[38] suggesting potential porosity. In addition, there are π···π stacking interactions between the pyridine ring and the aromatic ring, and between the aromatic ring and the aromatic ring with a center to center distance of 3.591(3) and 3.705(3) Å, respectively, which contribute to the stability of the molecular structure (Fig. S8).

### 3.3 Photochromic properties

The photochromic properties of **1** was studied. As shown in Fig. 2a, complex **1** exhibits distinct light-responsive color changes under 365 nm UV irradiation for 5 s and reached saturation after irradiation for 120 s (1P). Complex **1** demonstrates a remarkable chromatic transition from pale yellow to

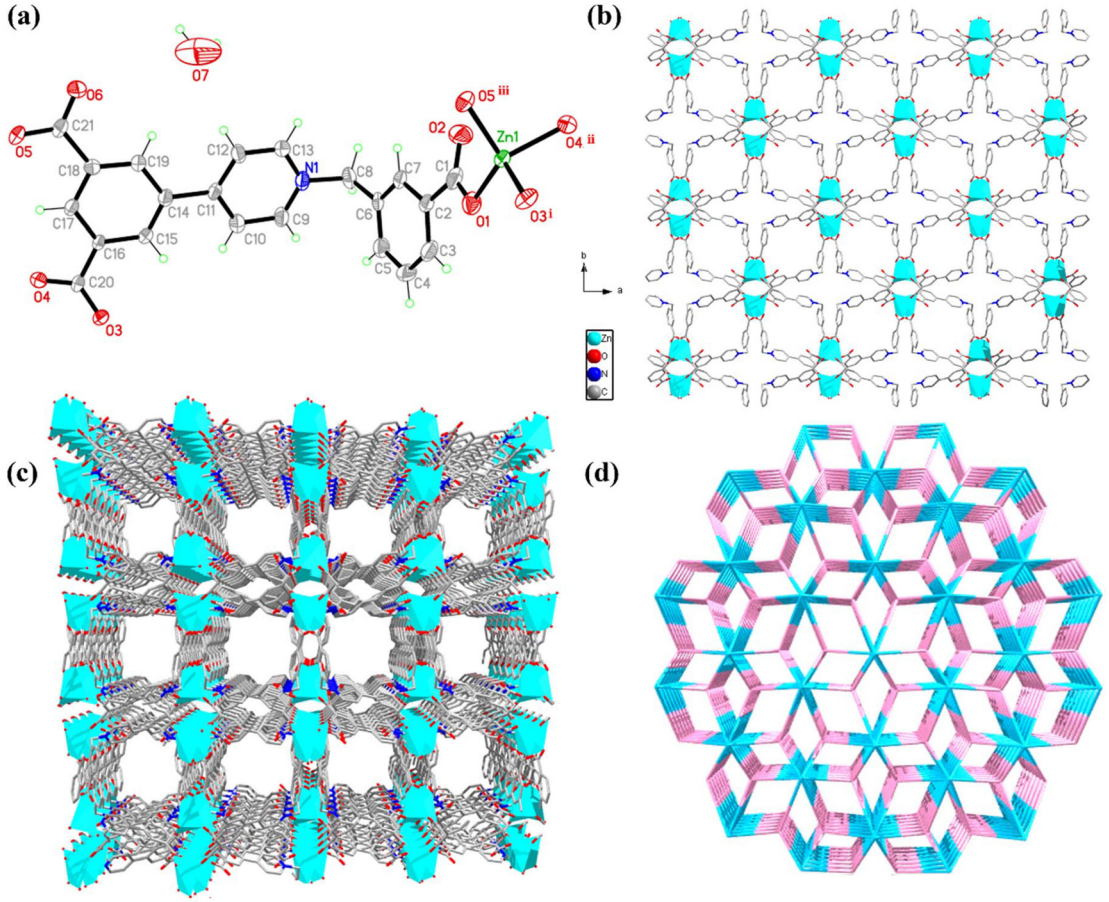


Fig. 1 (a) Coordination environment of **1** (i $-x + 1, y - 1, -z + 3/2$; ii $x - 1, y - 1, z$; iii $-x + 1, -y + 1, -z + 1$). (b) 2D structure of complex **1**. (c) 3D structure of **1**. (d) The topological network of complex **1**.

deep blue, the reversibility of photochromism differs significantly between the complex **1**. Complex **1P** achieves complete color recovery within 3 days under dark conditions. The photochromic processes of complex **1** was further recorded by IR and XRD. Structural integrity was confirmed through comparative analyses of IR and XRD patterns before and after irradiation, revealing no significant framework alterations (Fig. S1 and S9). This observation excludes irreversible structural isomerization or phase transitions as potential mechanisms. Solid-state UV-vis spectra further corroborate the photochromic behavior, with complex **1** displaying a prominent absorption band at 620 nm corresponding to radical formation (Fig. 2c). When the photochromic product (**1P**) is restored to the initial yellow state, the corresponding spectrum is also restored (Fig. S10). The reversible photochromic phenomenon of complex **1** can be repeated at least five times (Fig. S11). The changes of the complexes before and after irradiation were further detected by electron paramagnetic resonance (EPR) spectroscopy. As shown in Fig. 2d, complex **1** has no EPR signal before irradiation, and strong EPR signals appear at $g$ = 2.0042 after irradiation, confirming the generation of stable radical species through photoinduced electron transfer processes.

The photochromic properties of complex **1** modified by $Eu^{3+}$ and $Tb^{3+}$ (**Eu/Tb@Zn-MOF**) were also discussed. **Eu@Zn-MOF** and Tb@Zn-MOF showed photochromic behavior from white to light yellow upon irradiation by 365 nm UV light, and the color became saturated after irradiation within 7 min (Fig. 2b). Moreover, the fluorescence (365 nm) colors of **Eu@Zn-MOF** and **Tb@Zn-MOF** gradually changed from red to orange red and light green to yellow green, respectively (Fig. 2b). Both samples exhibited a gradual recovery to a white state upon heating at a temperature of 100 °C for a duration of 1 h. In addition, the decoloured sample demonstrated a shift in colour subsequent to re-irradiation, thereby suggesting that the colour alteration was reversible. Similarly, the photochromism of **Eu@Zn-MOF** and **Tb@Zn-MOF** was detected by solid-state UV-Vis spectroscopy. The samples of **Eu@Zn-MOF** and **Tb@Zn-MOF** showed a new absorption band at 600 nm after irradiation, and their intensity gradually increased with the increase of irradiation time, which indicated that the color of **Eu@Zn-MOF** and **Tb@Zn-MOF** gradually changed (Fig. S12).

The photochromic behavior observed in solid-state MOFs has been shown to primarily originate from photoinduced electron transfer processes. This phenomenon demonstrates critical dependence on the spatial arrangement of molecular

 

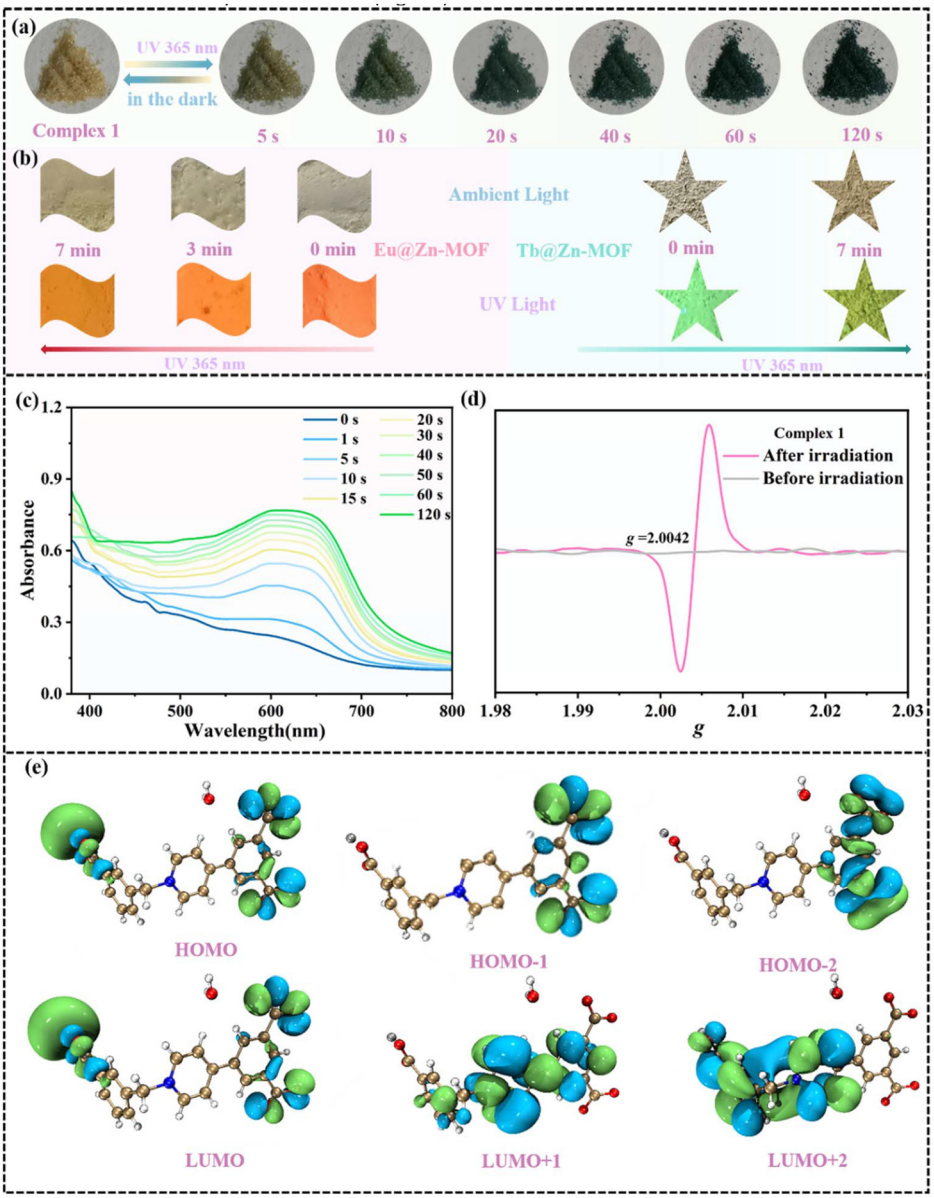


**Fig. 2** (a) Photographs of complex **1** before and after UV light irradiation. (b) Photographs of **Eu@Zn-MOF** and **Tb@Zn-MOF** before and after UV light irradiation. (c) UV-vis spectra of **1** for different UV irradiation durations. (d) EPR spectra of **1** before and after irradiation in the ambient environment. (e) Calculated molecular orbitals (HOMOs and LUMOs) of complex **1**.

components, where efficient electron transfer pathways are established through hydrogen bonding between electron-donating moieties and electron-accepting centers within the crystal lattice.[39,40] The possible electron-transferring hydrogen bonding information is listed in Table S3. For complex **1**, the oxygen atom O2, O3 and O5 from carboxylate group of $cbby^{2-}$ ligand are involved in hydrogen bonding with the carbon atom in the pyridinium ring (Fig. S13), which may construct the pathways of electron transfer. Moreover, the π···π interaction distance between the pyridine ring and the aromatic ring in complex **1** is 3.591(3) and 3.705(3) Å (Fig. S8), which facilitate the requirements for electron transfer upon UV-light irradiation. Further theoretical calculations were carried out to elucidate the potential mechanism of photoresponsive radical emission of complex **1**. As shown in Fig. 2e, the highest occupied molecular orbitals (HOMOs) of **1** are mainly located on the carboxyl groups and metal ions. The lowest unoccupied molecular orbital (LUMOs) of **1** is mainly located on the pyridine ring of $H_3cbby$ ligand, which indicates that the electron is transferred from the carboxyl oxygen atom to the pyridine nitrogen atom.

### 3.4 Luminescence properties

The photoluminescence properties of complexes **1**, **Eu@Zn-MOF** and **Tb@Zn-MOF** were studied in solid state at room temperature. As shown in Fig. S14, complex **1** shows intense

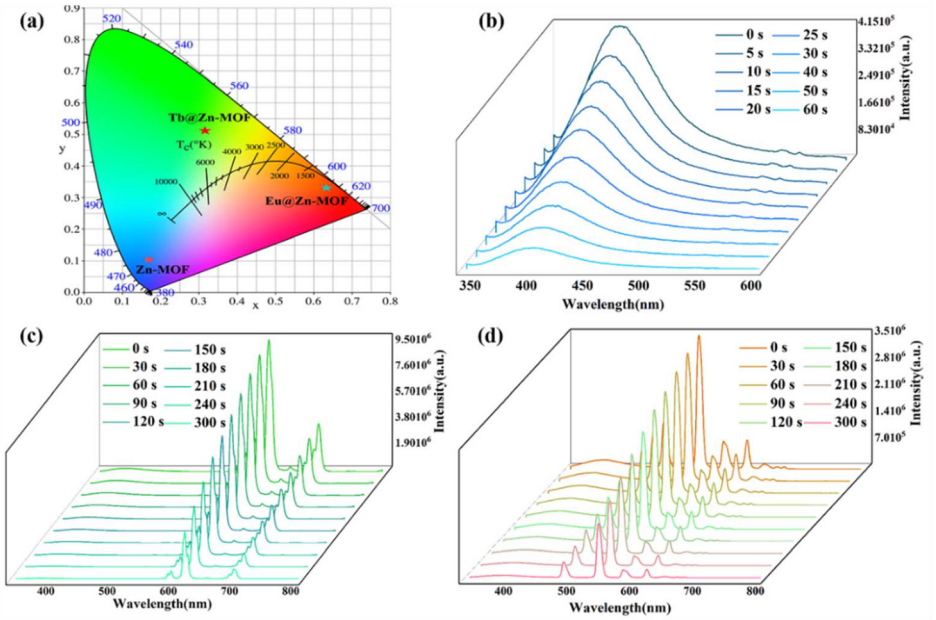


**Fig. 3** (a) CIE-1931 chromaticity diagram of complex **1**, **Eu@Zn-MOF** and **Tb@Zn-MOF**. Time-dependent photoluminescence spectra of complex **1** (b), **Eu@Zn-MOF** (c) and **Tb@Zn-MOF** (d) before and after irradiation.

strong emission peak at 400 nm when excited at 340 nm (CIE coordinates: 0.17, 0.10, Fig. 3a), while **Eu@Zn-MOF** and **Tb@Zn-MOF** displayed characteristic red and green luminescence, respectively, corresponding to the typical transitions of $Eu^{3+}$ ($^5D_0 \rightarrow {}^7F_4$) and $Tb^{3+}$ ($^5D_4 \rightarrow {}^7F$), which is consistent with the color indicated by the CIE coordinates (0.63, 0.33 of **Eu@Zn-MOF** and 0.32, 0.55 of **Tb@Zn-MOF**, Fig. 3a). Intriguingly, three complexes demonstrated photochromic behavior under light irradiation, accompanied by a gradual reduction in fluorescence intensity as their coloration deepened, suggesting that the fluorescence of complex **1**, **Eu@Zn-MOF** and **Tb@Zn-MOF** is quenched due to the formation of radicals (Fig. 3). Similarly, this reversible alternation between the two color states of the complex can be repeated at least five times without significantly reducing the color saturation or emission intensity (Fig. S15). These findings collectively establish complexes **1**, **Eu@Zn-MOF** and **Tb@Zn-MOF** as promising candidates for developing optically controlled luminescent switches, with potential applications in molecular sensing, anti-counterfeiting systems, and optoelectronic memory devices.

### 3.5 Detection of TC

The luminescent properties of complex **1** in water were evaluated. A uniform suspension was prepared by dispersing 10.0 mg of complex **1** in 30 mL of distilled water, followed by sonication for 30 min. The supernatant was then collected for fluorescence characterization. The emission spectrum of complex **1** in aqueous solution is shown in Fig. S16. No significant difference was observed in the fluorescence spectrum after soaking in water for 7 days (Fig. S17), confirming the good luminescence stability of its aqueous suspension. Given the strong fluorescence and high stability of complex **1**, its potential application for antibiotic detection was explored. Eight common antibiotics were selected for investigation (Fig. S18): theophylline (THEO), tiopronin (Tiopronin), L-dopa (L-DOPA), D-penicillamine (DP), riboflavin (RFN), aureomycin (CTC), terramycin (OTC), and tetracycline (TC). As shown in Fig. 4a, under identical conditions, complex **1** exhibited quenching rates of 30.2% and 32.8% for CTC and OTC, respectively, while the quenching efficiency for TC was significantly higher at 81.4%. This indicates that complex **1** functions as a promising fluorescent chemosensor for the specific detection of TC. The UV-vis spectra of eight antibiotics were compared with the spectra. As shown in Fig. S19, the UV-vis spectra of CTC, OTC and TC overlap greatly with the spectra of complex **1**, which indicates that the energy absorption of these three antibiotics has a certain effect on the change and quenching of fluorescence color.

To further evaluate the sensitivity of complex **1** towards TC, quantitative fluorescence (FL) titration experiments were performed by adding incremental amounts of a TC solution (1.00 mM) to the sample suspensions (Fig. 4b and c). The Stern–Volmer equation ($I_0/I = 1 + K_{SV}$ [M]) was applied to analyze the luminescence quenching, where $I_0$ and $I$ represent the emission intensities at 395 nm in the absence and presence of the analyte, respectively, $K_{SV}$ is the quenching constant, and [M] is the analyte concentration. The Stern–Volmer plot for TC was nearly linear at low concentrations (correlation coefficient = 0.9907), yielding a $K_{SV}$ value of $1.01 \times 10^4$ $M^{-1}$ (Fig. 4c). The limit of detection (LOD) for TC was calculated using the equation LOD = $3\sigma/m$, resulting in a value of

 

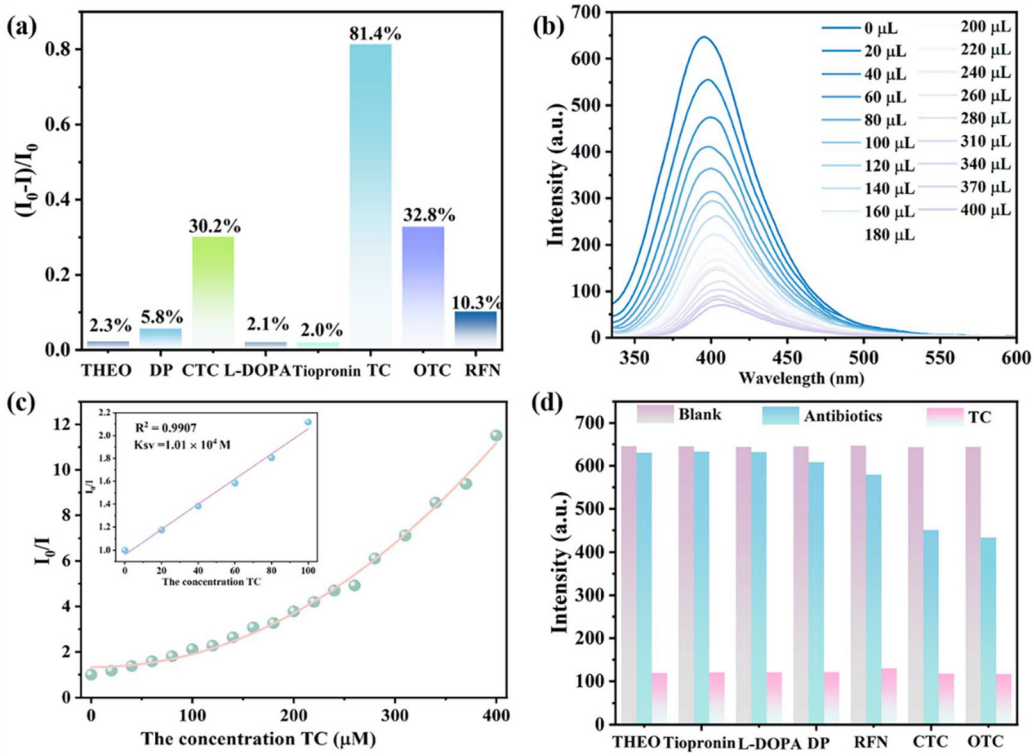


**Fig. 4** (a) Quenching efficiency of complex **1** in different antibiotic solutions. FL spectra (b) and Stern–Volmer plots (c) of complex **1** in different TC concentrations. (d) Quenching efficiency of complex **1** facing diverse antibiotics and TC.

0.72 μM. This LOD is superior to those of most reported MOF-based fluorescent chemosensors for TC detection (Table S4).

Given the importance of anti-interference capability for practical applications, complex **1** was tested for TC detection in the presence of TC and other antibiotics. As shown in Fig. 4d, the FL intensity of complex **1** decreased only slightly upon addition of other antibiotics but exhibited rapid decay upon contact with TC, indicating satisfactory anti-interference performance.

### 3.6 Degradation of TC

Given the promising detection performance of complex **1** in aqueous solution for TC, CTC, and OTC, its photocatalytic degradation capabilities towards these three antibiotics were further investigated. Standard solutions of each antibiotic were prepared at a concentration of 10 mg $L^{-1}$. Subsequently, 10 mg of complex **1** was ground into powder and added separately to 80 mL aliquots of each antibiotic solution. After stirring followed by a 30 min standing period for adsorption–desorption equilibrium, 5 mL of the suspension was centrifuged, and the supernatant absorbance ($C_0$) was measured to establish the initial concentration. A xenon lamp served as the light source for photocatalysis. At 10 min intervals over 100 min, 5 mL aliquots were sampled, centrifuged, and the absorbance of the supernatant was determined by UV-Vis spectrophotometry. As depicted in Fig. S20, the maximum absorption peaks of all three antibiotic solutions containing complex **1** decreased progressively with increasing irradiation time. Beyond 100 min, the changes in the absorption peaks became negligible, indicating that the degradation reaction had essentially reached completion. Fig. 5a shows that the degradation efficiencies of TC, OTC, and CTC by complex **1** reached 88.08%, 61.23%, and 14.13%, respectively, demonstrating its effectiveness in degrading these antibiotics, albeit with varying efficiencies.

Due to the high degradation efficiency of TC by complex **1**, this complex was selected for further study. The degradation efficiency was calculated using the formula: degradation efficiency = $C/C_0$, where $C_0$ and $C$ represent the initial and actual concentrations of tetracycline, respectively. As shown in Fig. 5b, under xenon lamp irradiation, TC concentration decreased sharply in the presence of complex **1**, achieving a degradation rate of 88.08% within 100 minutes. In contrast, control experiments conducted in the absence of light or complex **1** showed significantly slower degradation, resulting in much lower efficiencies of only 2.46% and 17.46%, respectively, under the same conditions. This performance of complex **1** surpasses that of most reported tetracycline-degrading materials (Table S5). Given the high degradation efficiency of TC by complex **1**, the photocatalytic activity of its $Eu^{3+}$ and $Tb^{3+}$-modified derivatives (**Eu@Zn-MOF** and **Tb@Zn-MOF**) towards TC degradation to evaluate the effect of modification was also studied to evaluate the modification effect. As shown in Fig. S21 and Fig. 5c, modification with $Eu^{3+}$ or $Tb^{3+}$ had no significant impact on the TC degradation rate compared to the

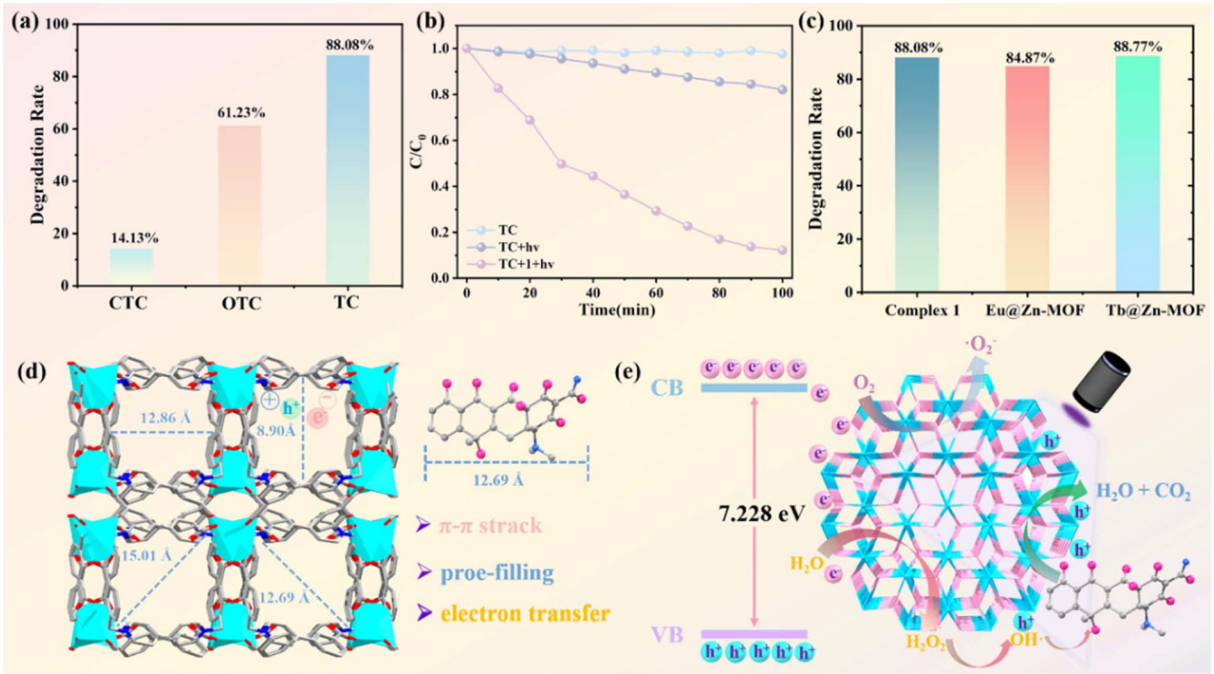


**Fig. 5** (a) Degradation rate of complex **1** in different antibiotic of CTC, OTC and TC. (b) Degradation line diagram of TC in complex **1**. (c) The degradation rate of TC by complex **1**, **Eu@Zn-MOF** and **Tb@Zn-MOF**. (d and e) Possible adsorption and photocatalytic mechanism of TC.

parent complex **1**. Collectively, these experiments demonstrate that complex **1**, **Eu@Zn-MOF**, and **Tb@Zn-MOF** can effectively accelerate the degradation of tetracycline.

The mechanism underlying the photocatalytic degradation was further elucidated. In complex **1**, the presence of abundant benzene and pyridine rings enables π–π stacking interactions with the benzene rings of TC, facilitating the adsorption of TC onto the complex.[41,42] Notably, the maximum dimension of the TC molecule (12.69 Å) is smaller than the pore size of complex **1**, and this appropriate pore size matching further enhances adsorption efficiency (Fig. 5d). Under xenon lamp irradiation, complex **1** generates a large number of photogenerated electrons ($e^-$) and holes ($h^+$). These charge carriers undergo separation (eqn (1)). Subsequently, photogenerated electrons migrate from the valence band (VB) to the conduction band (CB), where they reduce adsorbed $O_2$ to generate superoxide radicals ($^{\bullet}O_2^-$) (eqn (2)). Simultaneously, photogenerated holes can directly oxidize TC molecules, initiating their degradation (eqn (3)). The majority of the photogenerated holes ($h^+$) contribute directly to TC oxidation, a process that also promotes charge carrier separation by consuming holes (eqn (4)). A minor fraction of holes reacts with adsorbed $H_2O$ or surface hydroxyl groups to produce hydrogen peroxide ($H_2O_2$), which rapidly decomposes to yield hydroxyl radicals ($^{\bullet}OH$) (eqn (5)). These highly reactive $^{\bullet}OH$ radicals then further degrade TC (eqn (6)) (Fig. 5e).[43,44]

$$\text{Complex 1} + h\nu \rightarrow e_{CB}^- + h_{VB}^+ \quad (1)$$

$$e_{CB}^- + O_2 \rightarrow O_2^- \quad (2)$$

$$O_2^- + \text{TC} \rightarrow \text{degradation products} \quad (3)$$

$$h_{VB}^+ + \text{TC} \rightarrow \text{degradation products} \quad (4)$$

$$h_{VB}^+ + H_2O \rightarrow H_2O_2 + H^+ \rightarrow {}^{\bullet}OH \quad (5)$$

$$^{\bullet}OH + \text{TC} \rightarrow \text{degradad products} \quad (6)$$

Overall, the photocatalytic degradation of tetracycline proceeds *via* two primary pathways.[45,46] The first involves the initial attack of hydroxyl radicals ($^{\bullet}OH$), superoxide radicals ($^{\bullet}O_2^-$), or holes ($h^+$) on the tetracycline molecule, forming intermediates. Subsequent reactions, including dealkylation and ring-opening, ultimately lead to the mineralization products $H_2O$ and $CO_2$. The second pathway begins with the direct dealkylation of tetracycline, driven by the strong oxidizing power of $^{\bullet}O_2^-$ and $^{\bullet}OH$. Ring-opening reactions and terminal oxidation then occur, generating various intermediates before final conversion to $H_2O$ and $CO_2$ (Fig. S22).

### 3.7 Multiple intelligent anticounterfeiting applications

Leveraging the effective tetracycline degradation and adsorption capabilities of complex **1**, combined with the intense characteristic emissions of its $Eu^{3+}$/$Tb^{3+}$-modified forms (**Eu@Zn-MOF** and **Tb@Zn-MOF**), to explored the visual detection of TC using these materials. As illustrated in Fig. 6a, standard solutions of TC at varying concentrations were prepared and introduced into suspensions containing **Eu@Zn-MOF** or **Tb@Zn-MOF**. The samples were dried, and the resulting changes in fluorescence color were observed under 365 nm UV light. Under UV irradiation ($\lambda$ = 365 nm), pristine **Eu@Zn-MOF**

 

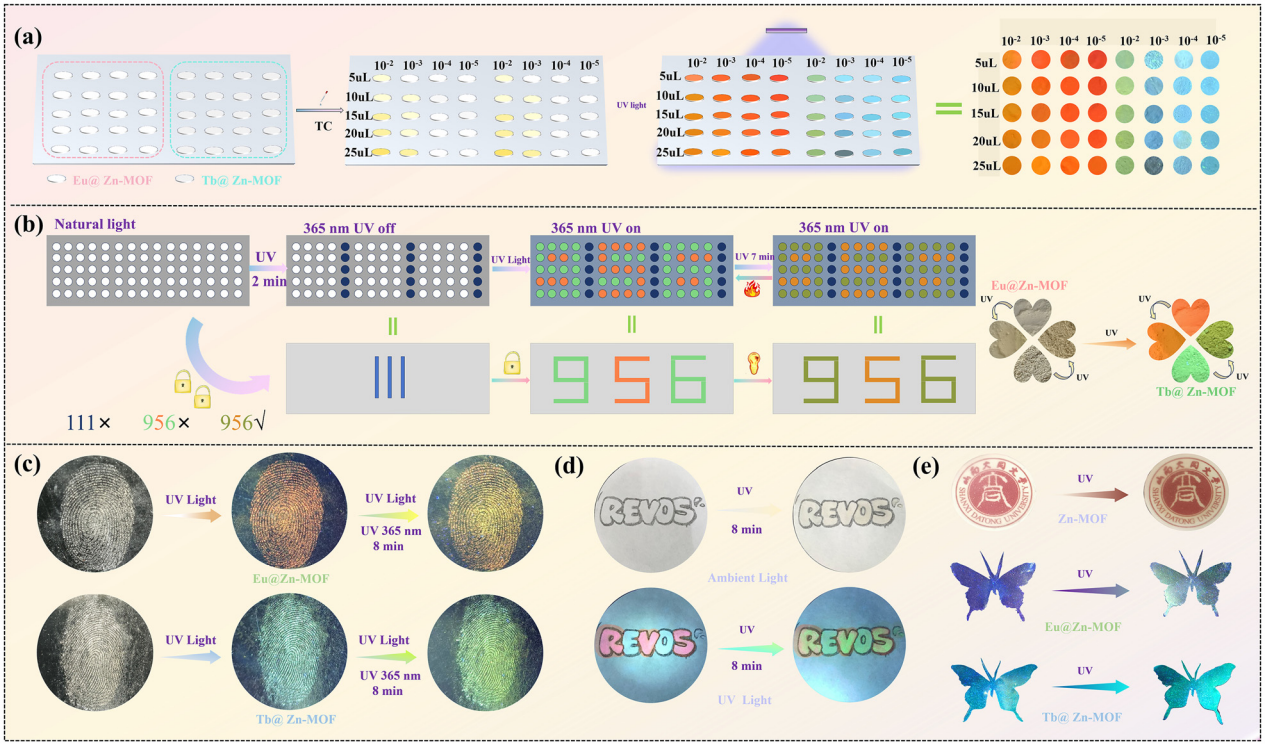


**Fig. 6** (a) Fluorescence response of **Eu@Zn-MOF** and **Tb@Zn-MOF** to different concentrations of TC. (b) Encryption and decryption based on multi-level information patterns and the corresponding three-layer security system. (c) Preparation of photochromic fluorescent fingerprints with **Eu@Zn-MOF** and **Tb@Zn-MOF** powders. (d) Inkless print photographs and fluorescent photographs of photochromic **Eu@Zn-MOF** and **Tb@Zn-MOF** based photochromism. (e) Photographs of PMMA-1 before and after irradiation and fluorescence photographs of PMMA-2 and PMMA-3 before and after irradiation.

and **Tb@Zn-MOF** exhibit bright red and green emissions, respectively. Upon dropwise addition of increasing concentrations of TC solution, the fluorescence color of **Eu@Zn-MOF** transitions from red to dark yellow, while that of **Tb@Zn-MOF** shifts from green to light blue. These distinct, concentration-dependent color changes demonstrate that **Eu@Zn-MOF** and **Tb@Zn-MOF** enable the visual detection of trace TC, highlighting their potential for developing portable TC detection devices.

The growing emphasis on information security in daily life has spurred the development of novel materials and technologies for encryption, anti-counterfeiting, and secure information storage. These systems utilize specific external stimuli (*e.g.*, temperature, light) for decryption, rendering encrypted information resistant to interpretation and replication. Leveraging the synergistic combination of reversible photochromism of complex **1** and the photoactivated fluorescence modulation of **Eu@Zn-MOF**/**Tb@Zn-MOF**, a dynamic anti-counterfeiting platform with spatial encryption capabilities was designed. As shown in Fig. 6b, the encryption matrix integrates complex **1**, **Eu@Zn-MOF** and **Tb@Zn-MOF**. Under continuous UV light, a bright "956" pattern emerges; extending irradiation to 7 min induces a gradual shift in fluorescence from red to orange-red (**Eu@Zn-MOF**) and from green to yellow-green (**Tb@Zn-MOF**). Crucially, the sequence and content of displayed patterns are dynamically programmable *via* UV exposure duration, enabling versatile information encryption. Thus, the authentic data ("956") achieves triple encryption through: (1) the neutral visible state, (2) the time-dependent photochromic pattern ("11"), and (3) the UV-activated fluorescent pattern ("956") with tunable emission.

Fingerprints, serving as unique biometric identifiers, are widely utilized in identity authentication systems. Capitalizing on this intrinsic uniqueness, researchers developed a novel anti-counterfeiting technology by integrating fingerprint patterns with the photoresponsive characteristics of lanthanide-functionalized metal–organic frameworks (**Eu/Tb@Zn-MOFs**). As shown in Fig. 6c, the process involves applying **Eu@Zn-MOF** powder onto a fingertip and then transferring the fingerprint onto adhesive tape to preserve the pattern. Remarkably, exposure to 365 nm UV irradiation under ambient conditions elicited dual-mode optical responses: the fingerprint visibly transitioned from white to light yellow while its fluorescence shifted from red to orange-red. Analogous experiments with **Tb@Zn-MOF** demonstrated comparable photochromic behavior, with the naked-eye color also transitioning from white to pale yellow and the fluorescence shifting from blue to yellow-green. This approach significantly enhances the application of fingerprints in both identification and anti-counterfeiting.

The synergistic integration of photochromism and tunable luminescence within **Eu/Tb@Zn-MOF** enables their deployment as smart optical tags for advanced anti-counterfeiting systems. As illustrated in Fig. 6d, suspensions of **Eu@Zn-MOF** and **Tb@Zn-MOF** were precisely cross-filled and coated to form a 'REVOS'-shaped module. Following 5 min of 365 nm UV irradiation, this module exhibited dual-mode authentication characteristics: its color transitioned from white to pale yellow, accompanied by diverse fluorescence color changes. This dynamic optical response, combined with the high spatial resolution afforded by the modular pattern, establishes the **Eu/Tb@Zn-MOF** composite as an excellent platform for high-security inkjet printing. This technology facilitates the encryption and storage of multi-dimensional information *via* photon/colorimetric dual-channel encryption.

To demonstrate the UV-responsive characteristics of these coordination systems, a series of photochromic films were prepared. Solutions of complex **1**, **Eu@Zn-MOF**, and **Tb@Zn-MOF** were separately prepared by dissolving each material with polymethyl methacrylate (PMMA) powder in an EtOH–$H_2O$ mixture (1 : 1, v/v, 5 mL). These solutions were then uniformly coated onto glass plates. After drying for 24 hours, hybrid matrix films were obtained: PMMA-1 (complex **1**), PMMA-2 (**Eu@Zn-MOF**) and PMMA-3 (**Tb@Zn-MOF**). As shown in Fig. 6e, PMMA-1 appears white and highly transparent. Following 3 min of 365 nm UV irradiation, its color shifts to light gray. Under identical conditions, PMMA-2 exhibits reversible luminescence switching from pink to yellow-green, while PMMA-3 demonstrates a transition from blue to blue-green. The discolored films revert to their original colors after 24 hours in the dark, mirroring the photochromic behavior observed in the powder samples. This reversibility indicates that the photochromism in the hybrid matrix films is may also attributed to the generation of free radicals.

## 4. Conclusion

In summary, a novel pyridinium-functionalized coordination complex **1** was synthesized, exhibiting reversible photochromism under UV light irradiation. Under 365 nm UV light irradiation, the photoresponse time of complex **1** is 5 s. Complex **1** can selectively detect TC in a variety of antibiotics with a detection limit of 0.72 μM. Due to the holes and photo-induced electron transfer of complex **1**, the degradation rate of tetracycline can be increased, and it can be degraded by 88.08% in 100 min. Notably, the porous architecture of Zn-MOF enabled efficient post-synthetic modification with $Eu^{3+}$/$Tb^{3+}$ ions, achieving rare compatibility between host photochromism and guest-derived lanthanide luminescence. This dual functionality was leveraged to develope **Eu/Tb@ZnMOF** as a bifunctional anti-counterfeiting material, where reversible color changes under UV irradiation coexist with excitation-dependent fluorescence switching. Moreover, **Eu/Tb@Zn-MOF** was developed into portable colorimetric test strips for real-time TC monitoring, where concentration-dependent color transitions enable rapid field detection. Furthermore, a hierarchical security platform integrating **1** (photochromic) and **Eu/Tb@Zn-MOF** (photochromic-fluorescent) was engineered, enabling multi-level authentication through orthogonal responses to light and UV observation—a significant advancement over conventional single-mode systems. This work not only provides mechanistic insights into stimulus-responsive behaviors of pyridinium-functionalized coordination but also pioneers a modular strategy for designing multifunctional MOF-based composites through combined metal–ligand selection and PSM engineering. The demonstrated applications in environmental remediation and advanced anti-counterfeiting systems highlight the material's versatility in addressing real-world challenges.

## Conflicts of interest

The authors declare no competing financial interest.

## Data availability

Data will be made available on request.

All data relevant to this study are available in the Supplementary Information, which contains materials and instrumentation, supplementary figures and X-ray crystallographic data (CIF). See DOI: **https://doi.org/10.1039/d5qi01641j**.

CCDC 2451117 contains the supplementary crystallographic data for this paper.[47]

## Acknowledgements

The authors acknowledge the financial support from the Natural Science Foundation of Shanxi Province (202403021222255 and 202403021212027).

## References

1 K. S. Blake, Y.-P. Xue, V. J. Gillespie, S. R. S. Fishbein, N. H. Tolia, T. A. Wencewicz and G. Dantas, The tetracycline resistome is shaped by selection for specific resistance mechanisms by each antibiotic generation, *Nat. Commun.*, 2025, **16**, 1452.

2 H. Wang, L. Wang, D. Li, K. Fan, Y. Yang, H. Cao, J. Sun, J. Ren, Y. Liu, L. Xiang, W. Li, M. Pan, H. Hu, Y. Chen, Z. Xu, Y. Huang, W. Wang and G. Pan, Uncovering the Molecular Landscape of Tetracycline Family Natural Products through Bacterial Genome Mining, *J. Am. Chem. Soc.*, 2025, **147**, 15100–15114.

3 J. Sivanesan, B. Sivaprakash, N. Rajamohan, V. S. S. Phanindra, C. Sonne, R. K. Liew and S. S. Lam, Remediation of tetracycline pollution using microplastics, green materials, membranes and sonocatalysts: a review, *Environ. Chem. Lett.*, 2024, **22**, 2943–2975.

 

4 Y. Zhao, J. Lin, Q. Wu, Y. Ying, J. Puigmartí-Luis, S. Pané and S. Wang, Revolutionizing Tetracycline Hydrochloride Remediation: 3D Motile Light–Driven MOFs Based Micromotors in Harsh Saline Environments, *Adv. Sci.*, 2024, **11**, 2406381.
5 V. T. Chu, A. Tsitsiklis, E. Mick, L. Ambroggio, K. L. Kalantar, A. Glascock, C. M. Osborne, B. D. Wagner, M. A. Matthay, J. L. DeRisi, C. S. Calfee, P. M. Mourani and C. R. Langelier, The antibiotic resistance reservoir of the lung microbiome expands with age in a population of critically ill patients, *Nat. Commun.*, 2024, **15**, 92.
6 Y. Mao, R. Xiong, J. Tian, G. Ling and P. Zhang, Advances and applications of metal–organic framework/molecularly imprinted polymer (MOF/MIP) for fluorescence detection, *Coord. Chem. Rev.*, 2025, **537**, 216691.
7 W. Sun, Y. Huo, X. Feng, L. Wei, X. Lu, S. Liu and Z. Gao, Recent advances in metal-organic frameworks (MOFs)-based colorimetric sensors for visual detection of food freshness, *Coord. Chem. Rev.*, 2025, **535**, 216638.
8 E. J. N. Muzii, Detection by fluorescence of oxytetracycline bound to bone, *Nature*, 1961, **189**, 934–935.
9 J. Li, R. Yao, B. Deng, Z. Li, K. Tuo, C. Fan, G. Liu and S. Pu, A facile construction of bifunctional core–shell–shell structured magnetic metal–organic frameworks for detection and removal of tetracycline, *Chem. Eng. J.*, 2023, **464**, 142626.
10 J. Sun, H. Wu, C. Fu, C. Zhang, Z. Hu and M. Zhou, Novel Fenton-like system based on bifunctional MgO/g-$C_3N_4$ S-scheme heterojunction photoanode for efficient tetracycline degradation, *Appl. Catal., B*, 2024, **351**, 123976.
11 J. Zeng, W. Xie, Y. Guo, T. Zhao, H. Zhou, Q. Wang, H. Li, Z. Guo, B. B. Xu and H. Gu, Magnetic field facilitated electrocatalytic degradation of tetracycline in wastewater by magnetic porous carbonized phthalonitrile resin, *Appl. Catal., B*, 2024, **340**, 123225.
12 Abhivyakti, P. Kaur, D. Aggarwal, Nitansh and S. Singhal, Defect-engineered C,N-ZnO,/$Co_3O_4$/$CoFe_2O_4$/$Fe_3O_4$ for ultra-fast tetracycline degradation and environmental impact assessment using an in silico mathematical model, *Adv. Compos. Hybrid Mater.*, 2025, **8**, 156.
13 X. Bai, J. Xing, X. Huang, S. Sun, N. Wang, T. Wang and H. Hao, N-heterocyclic COFs regulate p-π conjugation to realize electron acceleration effect and achieve self-Fenton degradation of chloramphenicol, *Chem. Eng. J.*, 2025, **513**, 162782.
14 C. Luo, J. Xiong, H. Zeng and M. Liao, Polyaniline-ZnTi-LDH heterostructure with d–π coupling for enhanced photocatalysis of pollutant removal, *J. Colloid Interface Sci.*, 2025, **684**, 792–804.
15 T. Liu, W. Zhao, S. Meng, B. Dong, N. Shi and W. Shi, Multifunctional Zn–carbon dots enhanced specific recognition and in situ degradation of tetracycline, *J. Mater. Chem. C*, 2025, **13**, 4594–4604.
16 N. Dhenadhayalan, K. Lin and T. A. Saleh, Recent Advances in Functionalized Carbon Dots Toward the Design of Efficient Materials for Sensing and Catalysis Applications, *Small*, 2020, **16**, 1905767.
17 M. Crippa, C. Perego and G. M. Pavan, Non-trivial stimuli-responsive collective behaviours emerging from microscopic dynamic complexity in supramolecular polymer systems, *Nat. Commun.*, 2025, **16**, 5030.
18 Y. Sheng, Q. Gui, Y. Zhang, X. Yang, F. Xing, C. Liu, Y. Di, S. Wei, G. Cao, X. Yang, X. Zhang, Y. Liu and Z. Gan, Lead–Free Perovskites with Photochromism and Reversed Thermochromism for Repeatable Information Writing and Erasing, *Adv. Funct. Mater.*, 2024, **34**, 2406995.
19 X. Song, X. Liu, D. Zhang, J. Liao, S. Zhu and W. Zheng, High-Contrast Thermochromism in Room-Temperature Transparent Layered Perovskite PEA2PbBr4 with a High Temperature-Induced Bandgap Change Rate of 0.8 meV/K, *J. Am. Chem. Soc.*, 2024, **146**, 24670–24680.
20 J. Wang, Y. Yang, L. Zhang and Z. Li, Engineering Organic Photochromism with Photoactivated Phosphorescence: Multifunctional Smart Devices and Enhanced Four–Channel Data Storage, *Adv. Mater.*, 2025, 2503074.
21 D. Zhao, Z. Li, Q. Li, Y. Wang and H. Li, Design, classification, and applications of organic, luminescent lanthanide-based photoresponsive materials: A review, *Coord. Chem. Rev.*, 2025, **540**, 216770.
22 J. Shao, S. Feng, M. Liu, Y. Guo, C. Lu, S. Ke, H. Sun, D. Tu, D. Peng, Q. Zhang and F. Liu, romising Coloration Composite Strategy to Multicolor Photochromism for On–Demand Information Displays, *Adv. Funct. Mater.*, 2025, 2425059.
23 J. Huang, L. Tu, H. Huang, H. Wei, Q. Zhang and B. Zhou, Manipulating energy migration in nanoparticles toward tunable photochromic upconversion, *Nat. Commun.*, 2024, **15**, 10890.
24 H. Kong, J. Y. Wang, J. C. Liu, L. Zhang, P. Y. Liao, Y. Q. Qi, Z. Liu, S. G. Wu and M. L. Tong, Photochromic Dysprosium Single–Molecule Magnet Featuring Reversible Redox Transformation of Polyoxomolybdate Moiety, *Angew. Chem., Int. Ed.*, 2025, **64**, e202422557.
25 Q. P. Qin, J. Lu, C. Sun, M. S. Wang and G. C. Guo, Design Strategy for Improving Detection Sensitivity in a Bromoplumbate Photochromic Semiconductor, *Small*, 2024, **20**, 2307333.
26 F. Hassan, Y. Tang, H. K. Bisoyi and Q. Li, Photochromic Carbon Nanomaterials: An Emerging Class of Light–Driven Hybrid Functional Materials, *Adv. Mater.*, 2024, **36**, 2401912.
27 B. Garai, G. Das, C. M. Duncan, H. F. Nour, F. Benyettou, T. Prakasam, S. Varghese, H. I. Hamoud, M. El-Roz, J. I. Martinez, F. Gándara, M. A. Olson and A. Trabolsi, Triple energy conversion cascade in a densely charged redox active covalent organic actuator, *Nat. Commun.*, 2025, **16**, 5083.
28 S. T. Burton, G. Lee, C. E. Moore, C. S. Sevov and C. Turro, Cyclometallated Co(III) Complexes with Lowest-Energy Charge Transfer Excited States Accessible with Visible Light, *J. Am. Chem. Soc.*, 2025, **147**, 13315–13327.
29 P. X. Li, X. D. Guo, Y. H. Sun and G. C. Guo, Visualization of Light–Induced Rotational Movement in Crystal:

Exploring the Mechanism of Viologen–Containing Molecular Machines, *Small*, 2025, **21**, 2409285.

30 H. Chen, X. Yang, Y. Ye, H. Hong, Q. Wei, Y. Zhu and M. J. Lin, Ultrabright and Water–Stable Eu(III)–Based MOF Scintillators Sensitized by Dual–Antenna Ligands for Real–Time and Underwater X–Ray Imaging, *Angew. Chem., Int. Ed.*, 2025, e202506118.

31 H. L. Wang, Y. L. Li, H. H. Zou, F. P. Liang and Z. H. Zhu, Smart Lanthanide Metal–Organic Frameworks with Multicolor Luminescence Switching Induced by the Dynamic Adaptive Antenna Effect of Molecular Rotors, *Adv. Mater.*, 2025, 2502742.

32 J. Wang, Z. Gao, Y. Jia, X. Tong, Y. Zhou, F. Hu and Y. S. Zhao, MAPbBr3 Quantum Dots Encapsulated Within Lanthanide–MOFs for Time–Resolved Multicolor Dynamic Anticounterfeiting, *Adv. Mater.*, 2025, **37**, 2501271.

33 J. I. Deneff, L. E. S. Rohwer, K. S. Butler, B. Kaehr, D. J. Vogel, T. S. Luk, R. A. Reyes, A. A. Cruz-Cabrera, J. E. Martin and D. F. Sava Gallis, Orthogonal luminescence lifetime encoding by intermetallic energy transfer in heterometallic rare-earth MOFs, *Nat. Commun.*, 2023, **14**, 981.

34 Z. Li, X. B. Li, M. E. Light, A. E. Carrillo, A. Arauzo, M. Valvidares, C. Roscini, F. Teixidor, C. Viñas, F. Gándara, E. Bartolomé and J. G. Planas, A Metal–Organic Framework Incorporating Eight Different Size Rare–Earth Metal Elements: Toward Multifunctionality À La Carte, *Adv. Funct. Mater.*, 2023, **33**, 2307369.

35 X. Xu and B. Yan, Bionic Luminescent Skin as Ultrasensitive Temperature–Acoustic Sensor for Underwater Information Perception and Transmission, *Adv. Mater.*, 2024, **36**, 2309328.

36 D.-D. Yang, H.-W. Zheng, Y.-H. Fang, Q.-F. Liang, Q.-Z. Han, Y.-S. Shi and X.-J. Zheng, Multistimuli-Responsive Materials Based on Zn(II)-Viologen Coordination Polymers and Their Applications in Inkless Print and Anticounterfeiting, *Inorg. Chem.*, 2022, **61**, 7513–7522.

37 T. Gong, P. Li, Q. Sui, J. Chen, J. Xu and E.-Q. Gao, A stable electron-deficient metal–organic framework for colorimetric and luminescence sensing of phenols and anilines, *J. Mater. Chem. A*, 2018, **6**, 9236–9244.

38 A. L. Spek, PLATONSQUEEZE: a tool for the calculation of the disordered solvent contribution to the calculated structure factors, *Acta Crystallogr., Sect. C:Struct. Chem.*, 2015, **71**, 9–18.

39 D.-D. Yang, T. Xiao, Y.-Y. Yang, J.-H. Xue, Y.-S. Shi, Q. Ma and X.-J. Zheng, Two viologen-based complexes as persistent luminescent materials and their applications in inkless print and anticounterfeiting, *Chem. Eng. J.*, 2024, **488**, 151047.

40 D.-D. Yang, F.-Q. Meng, Y.-S. Shi, T. Xiao, Y.-H. Fang, H.-W. Tan and X.-J. Zheng, A series of zinc coordination compounds showing persistent luminescence and reversible photochromic properties via charge transfer, *Chem. Eng. J.*, 2023, **466**, 143202.

41 X. Zhao, Q. Li, P. Pachfule, Z. Wang, S. Liu, W. Wu, M. Wu and A. Thomas, Construction of Covalent Organic Framework Nanofiber Membranes for Efficient Adsorption of Antibiotics, *Small*, 2023, **19**, 2301200.

42 I. Ahmed, G. Lee, H. J. Lee and S. H. Jhung, Adsorption of pharmaceuticals from water using metal-organic frameworks (MOFs), MOF-derived carbons, covalent-organic frameworks (COFs), COF-derived carbons: Comparison of the four adsorbents, *Chem. Eng. J.*, 2024, **488**, 151022.

43 Y. Cao, Y. Wang, S. Wei, M. Li, H. Wang, F. Zhou, J. Li and J. Huang, Substituted triazine-based covalent organic frameworks aerogels for the efficient adsorption and catalytic degradation of tetracycline hydrochloride, *J. Colloid Interface Sci.*, 2025, **686**, 978–989.

44 X. Bai, R. Liu, Z. Wei and M. Liu, N-heterocyclic COFs regulate p-π conjugation to realize electron acceleration effect and achieve self-Fenton degradation of chloramphenicol, *Appl. Catal., B*, 2025, **378**, 125564.

45 R. Cheng, J. Ren, H. Wang, H. Liang and P. Tsiakaras, Modified-pollen confined hybrid system: A promising union for visible-light-driven photocatalytic antibiotic degradation, *Appl. Catal., B*, 2024, **352**, 124024.

46 Z. Zhang, J. Liang, W. Zhang, M. Zhou, X. Zhu, Z. Liu, Y. Li, Z. Guan, C.-S. Lee, P. K. Wong, H. Li and Z. Jiang, Photo-induced $CO_2$ cycloaddition and tetracycline degradation over novel FeOx modified defective graphitic carbon nitride composite, *Appl. Catal., B*, 2023, **330**, 122621.

47 J.-H. Xue, D.-D. Yang, Y.-S. Shi, Y.-Y. Yang, Y.-J. Bai, Q. Ma and X.-J. Zheng, CCDC 2451117: Experimental Crystal Structure Determination, 2025, DOI: **10.5517/ccdc.csd.cc2n8l9v**.

 